Directional solidification of Cu with dispersed W nanoparticles: A molecular dynamics study in the context of additive manufacturing

Quentin Bizot, Olivier Politano, Florence Baras, Vladyslav Turlo

MTLA 36 (2024) 102140

Contents lists available at ScienceDirect

Materialia

journal homepage: www.elsevier.com/locate/mtla

Full length article

Directional solidification of Cu with dispersed W nanoparticles: A molecular dynamics study in the context of additive manufacturing

Q. Bizot [a], O. Politano [a,*], F. Baras [a,*], V. Turlo [b,*]

[a] Laboratoire Interdisciplinaire Carnot de Bourgogne, UMR 6303 CNRS-Université de Bourgogne, 9 Avenue A. Savary, Dijon, France
[b] Empa - Swiss Federal Laboratories for Materials Science and Technology, Laboratory for Advanced Materials Processing, Feuerwerkerstrasse 39, Thun, 3602, Switzerland

ARTICLE INFO

Keywords:
Directional solidification
Molecular dynamics simulations
Heterogeneous nucleation
Metal matrix composites

ABSTRACT

Directional solidification, resulting in the development of columnar grains, is prevalent in laser-additive manufacturing of metal parts. The addition of grain refiners or inoculants enables the control of the nucleation process and columnar-to-equiaxed transition. In this study, we applied molecular dynamics simulations to investigate the directional solidification in liquid copper inoculated with tungsten nanoparticles. The interaction of the solidification front with inert nanoparticles resulted in either their engulfment in the Cu matrix or their pinning by grain boundaries. Analysis of the forces acting on the nanoparticles and the temperature field provides conditions for engulfment, determining the feasibility of copper matrix composites. By global cooling reflecting the thermal dynamics characteristics of additive manufacturing, a columnar-to-equiaxed transition can be captured at the nanoscale, with heterogeneous nucleation occurring at the nanoparticle surfaces. The conditions for the onset of heterogeneous nucleation were assessed on the basis of nanoparticle size and interpreted in terms of classical nucleation theory. Our results highlight the critical role of W-nanoparticle wetting by Cu solid grains in increasing grain refinement efficiency and suppression of columnar growth in additive manufacturing.

1. Introduction

Laser additive manufacturing is a layer-by-layer fabrication technique for metal parts with customized geometry, characterized by a close connection between material, processing conditions, solidification microstructure, and resulting part performance [1]. The high energy density of a laser combined with the high thermal conductivity of metals leads to the appearance of extreme temperature gradients across the solid–liquid interface, leading to directional solidification and the development of columnar grains. Such a type of microstructure is undesirable because of the promotion of hot and cold cracking, which also leads to anisotropic behavior and poor mechanical performance of the fabricated parts. To achieve the columnar-to-equiaxed transition during solidification, a specific cooling rate threshold must be reached to achieve the degree of undercooling necessary for grain nucleation to take place [2]. One method of controlling the nucleation process at lower degrees of undercooling and achieving a fine, uniform (or functionally graded) equiaxed grain structure without cracks is adding to the melt grain refiners commonly in the form of nanoparticles made of refractory materials [3,4]. If such nanoparticles have a tendency to dissolve (and eventually melt due to size effects), heterogeneous nucleation is promoted without nanoparticles left in the matrix, leading to the fabrication of functionally graded materials [5]. Otherwise, nanoparticle-reinforced metal matrix composites are fabricated, with the best mechanical performance achieved under a uniform distribution of nanoparticles throughout the material [6]. Such a uniform distribution is defined by (1) the inoculation effect of nanoparticles, i.e. their ability to promote grain nucleation before interaction with the solidification front, and (2) by the interactions between nanoparticles and the solidification front. In the latter, two situations can occur: either the particle is engulfed/captured by the solidification front, or it is pushed further by it. In both scenarios, the morphology of the front is altered when it encounters a particle. The microstructure of the solidified material will also differ significantly: the pushing of particles results in a clustering/agglomeration effect, while the engulfment of particles leads to their dispersion throughout the matrix. The critical velocity of the solidification front leading to the engulfment/pushing transition has been the subject of numerous studies, with a summary of the phenomenological models provided in the work of Youssef et al. [7].

In this work, we focus on the microscopic aspects of directional solidification in copper with dispersed inclusions of W nanoparticles

* Corresponding authors.
E-mail addresses: olivier.politano@u-bourgogne.fr (O. Politano), fbaras@u-bourgogne.fr (F. Baras), vladyslav.turlo@empa.ch (V. Turlo).

https://doi.org/10.1016/j.mtla.2024.102140
Received 25 March 2024; Accepted 28 May 2024
Available online 30 May 2024

Table 1
Pure Cu properties calculated with the EAM interatomic potential [14] and compared with experimental values, ab initio values (*) at 0 K, or Thermo-Calc data (**). Temperature-dependent parameters are evaluated at the Cu melting temperature T_m. †Cohesion energies are evaluated at 0 K.

Properties	Symbol	MD	Exp/*Ab initio*
bulk melting temperature	T_m	1181 K	1358 K
lattice parameter Cu	$a(T_m)$	0.37362 nm	0.36907 nm
cohesive energy Cu-*fcc*†	$E_0(fcc)$	−3.540 eV/atom	−3.54* eV/atom [15]
hcp-fcc energy difference	$E_0(hcp)$-$E_0(fcc)$	0.011 eV/atom	0.009* eV/atom [16]
atomic volume Cu	$\Omega = a(T_m)^3/4$	13.04×10^{-30} m^3	12.57×10^{-30} m^3
atomic mass Cu	m_0	1.055×10^{-25} kg	1.055×10^{-25} kg
solid/liquid interface energy	γ_{SL}	110 mJ m^{-2}	256 mJ m^{-2} [17]
bulk latent heat of fusion	L_V	1.122×10^9 J m^{-3}	1.51×10^9 ** J m^{-3}
heat conductivity liquid	κ_{Cu}	1.32 W m^{-1} K^{-1}	150.49 W m^{-1} K^{-1} [18]
heat capacity solid Cu	$C_{p,s}$	439 J kg^{-1} K^{-1}	480.9 J kg^{-1} K^{-1} [19]
heat capacity liquid Cu	$C_{p,l}$	440 J kg^{-1} K^{-1}	531.5 J kg^{-1} K^{-1} [19]
density Cu (solid)	$\rho = m_0/\Omega$	8.09 10^3 kg m^{-3}	8.96×10^3 kg m^{-3} [19]
heat diffusivity Cu	$D_{th} = \kappa/\rho C_p$	3.829 10^{-7} m^2 s^{-1}	3.16 10^{-5} m^2 s^{-1}
kinematic viscosity Cu	η	4.18 10^{-3} kg s^{-1} m^{-1}	4.0 10^{-3} kg s^{-1} m^{-1} [20]

Table 2
Pure W properties were calculated with the EAM interatomic potential [14] and compared with experimental values. Temperature-dependent parameters are evaluated at the Cu melting temperature T_m.

Properties	Symbol	MD	Exp
lattice parameter W	$a(T_m(\text{Cu}))$	0.318 nm	0.3179 nm [21]
atomic volume W	Ω	16.08 10^{-30} m^3	16.06 10^{-30} m^3
atomic mass W	m_0	3.053×10^{-25} kg	3.053×10^{-25} kg
heat conductivity W	κ_W	10.49 W m^{-1} K^{-1}	115.23 W m^{-1} K^{-1} [21]
heat capacity solid W	$C_{p,s}$	76.87 J kg^{-1} K^{-1}	149.84 J kg^{-1} K^{-1} [21]
density W (solid)	$\rho = m_0/\Omega$	1.90 10^4 kg m^{-3}	1.90 10^4 kg m^{-3}
heat diffusivity W	$D_{th} = \kappa/\rho C_p$	3.42×10^{-6} m^2 s^{-1}	4.05×10^{-5} m^2 s^{-1} [21]

(W-NPs). Due to its high thermal/electrical conductivity, copper has many applications in heat exchangers, microelectronics, etc., which would benefit from the flexibility offered by additive manufacturing methods [8]. However, copper is prone to the formation of columnar grains and solidification cracks during laser processing, reducing its mechanical performance [9]. Thus, copper could benefit significantly from the introduction of nanoscale inoculants and strengthening agents during laser additive manufacturing, which could not only improve its strength and ductility but also maintain its high electrical conductivity [10]. As a refractory metal, tungsten exhibits high strength and low melting point depression, combined with near-complete immiscibility with copper. In this regard, tungsten nanoparticles can serve as solid and inert grain entities in copper, which have already been shown to improve the mechanical strength [11], high-temperature creep resistance [12], and thermal stability against grain growth [13]. Despite all these benefits, no attempts have been made in the past to isolate and characterize the effect of W-NPs on the nucleation and solidification of copper, in particular, at extreme temperature gradients relevant to laser additive manufacturing processes.

To fill this gap, we examined the directional solidification with and without cooling of the liquid Cu containing dispersed W-NPs. To achieve this goal, large-scale molecular dynamics simulations were conducted and employed as *in-situ* tools to investigate the elemental mechanisms associated with such solidification processes. This approach presents an intriguing alternative to experimental observations that can be challenging to implement at the nanoscale. Moreover, molecular dynamics simulations were proven tools to isolate and investigate in detail nucleation [22–26] and directional solidification [23,27,28] in metals and alloys, with simulation results of directional solidification often used to parametrize larger-scale phase field models [29–32]. Our current work is in continuation of our previous work on the nanoscale directional solidification of pure Ni [33], which was the first study to implement additional melt cooling to compensate for the lack of conductive cooling associated with electronic thermal transport. This is a systematic error in molecular dynamics simulations of metals, leading to orders of magnitude lower thermal conductivities compared to the experimental ones. We demonstrated that such compensatory cooling is instrumental in capturing grain nucleation ahead of the solidification front, at the essence of columnar-to-equiaxed transition.

Here, for the first time, we will uncover the effect of the temperature gradient and cooling rate on solidification front interactions with inoculant NPs. We compare our results with existing theories, defining their limits of applicability at the nanoscale.

2. Methods

The molecular dynamics simulations were carried out using the Large-scale Atomic Molecular Massively Parallel Simulator (LAMMPS) software [34] with the embedded atom method (EAM) potential developed by Wei et al. [14] for the Cu-W system. The potential captures well the Cu/W immisibility and the stability of the W nanoparticles at elevated temperatures, with other properties relevant to the solidification process estimated at the copper melting point and presented in Tables 1 and 2. The methodologies used to calculate the various quantities are described in detail in our previous articles [33,35]. The experimental data from the literature is also reported in such tables for comparison. Reasonable agreements are found for all quantities except thermal conductivity. Thermal conductivity calculated by MD estimates only the contribution of phonons, and not that of electrons. The way we propose to correct such a flaw is by imposing an extra cooling rate in addition to a temperature gradient, as explained later. The simulation data are processed and visualized using the OVITO

software [36], with the local atomic structure and grain orientation determined using Polyhedral Template Matching [37].

The model geometry used in the present work was inspired by our previous work [33], and is depicted in Fig. 1. We considered a quasi-3D system in a simulation box of $100\times1.4\times200$ nm^3. Atomsk software [38] was used to construct polycrystalline samples composed of 25 columnar grains. Each grain had its [010] axis aligned with the y direction and rotated randomly in the xz plane. Periodic boundary conditions were applied in the x and y directions, but not in the z direction, which is shrink-wrapped. The y direction was slightly larger than twice the cut-off distance of the interatomic potential to avoid multiple interactions through periodic boundaries. The system was divided into three regions along the z direction: a lower region located between 0 and 20 nm kept at a fixed temperature and named the substrate, a middle region from 20 to 50 nm, and an upper region that was effectively affected by the laser beam (in relevance to a melt pool in the additive manufacturing processes) and named the laser region.

The first model (called later model A) was considered as follows. First, the complete system was equilibrated in the NPT (isothermal–isobaric) ensemble for 200 ps at 300 K and zero pressure. A further equilibration in the NVT (canonical) ensemble is applied for 100 ps. Then, the substrate region was kept at 300 K, while the temperature of the laser region was set at 1230 K for 2 ns. The value of the temperature in the laser region was chosen slightly above the Cu melting temperature to allow its melting. Between substrate and laser regions, the atoms can evolve freely, essentially establishing an initial temperature gradient. After 2 ns, the laser heating was removed but the substrate was kept at 300 K until the end of the simulation. Atoms in regions above the substrate were integrated into the NVE ensemble. This procedure allowed us to observe the evolution of a solid/liquid interface in an evolving temperature gradient. Ten W-NPs of equal size were randomly distributed in the laser region. Three simulations were performed with different nanoparticle sizes, namely 1.58 nm, 3.16 nm, and 6.32 nm. A reference simulation without NPs was also conducted. This model is designed to study the effect of temperature gradient on solidification kinetics and solidification front interactions with secondary phase nanoparticles in the absence of heterogeneous nucleation.

In a second model (called later model B), we applied the same initial equilibration as in model A, but the laser region temperature was set at 1250 K whereas the substrate region temperature was set at 900 K for 2 ns. After this initial stage, the laser thermostat was removed and replaced by a temperature ramp corresponding to a cooling rate of 175 K/ns. The substrate temperature was kept at 900 K until the end of the simulation. In this model, a single W-NP was introduced in the laser region. Five particle radii were considered R_1 = 3.18 nm = 10 lattice units (l.u.), R_2 = 6.36 nm = 20 l.u., R_3 = 9.55 nm = 30 l.u., R_4 = 12.72 nm = 40 l.u., and R_5 = 15.90 nm = 50 l.u. Two orientations of the W-NP along the z direction were investigated, namely [101] and [001]. This model was designed to capture and study in detail the heterogeneous nucleation, while avoiding extreme effects of temperature gradient.

3. Results and discussion

3.1. Model A — Simulation results

After the first equilibration steps are completed, the time is reset to zero. At this timestep, the samples can be separated into three parts considering the temperature differences (as shown in Fig. 2). The substrate part up to 20 nm is maintained at a constant temperature of 300 K. The middle part features a relatively steep temperature gradient, and the final part converges to the plateau while approaching the free surface. However, when considering the microstructure analysis, only two (solid and liquid) parts emerge. The *fcc* fraction (dashed line) close to 1 corresponds to the solidified region while the fraction close to zero corresponds to the liquid phase. Slight deviations from 1 in the solidified part correspond to grain boundaries, while larger deviations correspond to the presence of W particles. At t = 0 ns, we can also confirm that the W-NPs remained solid and spherical, and no changes in size from the initial one i.e. no dissolution took place in the melt. Furthermore, the polycrystalline structure (as shown in the snapshot) in the solid Cu region above the substrate region experienced substantial grain growth with remaining grain boundaries aligned with the direction of the temperature gradient i.e., z direction. In laser material processing, such a region with coarser grains in the vicinity of the melt pool is referred to in the literature as a heat-affected zone (HAZ) [9]. Interestingly, the leftmost grain boundary coincides with the W nanoparticle in the solid Cu, which might be an indication of Zener pinning, reported experimentally in such a system [13].

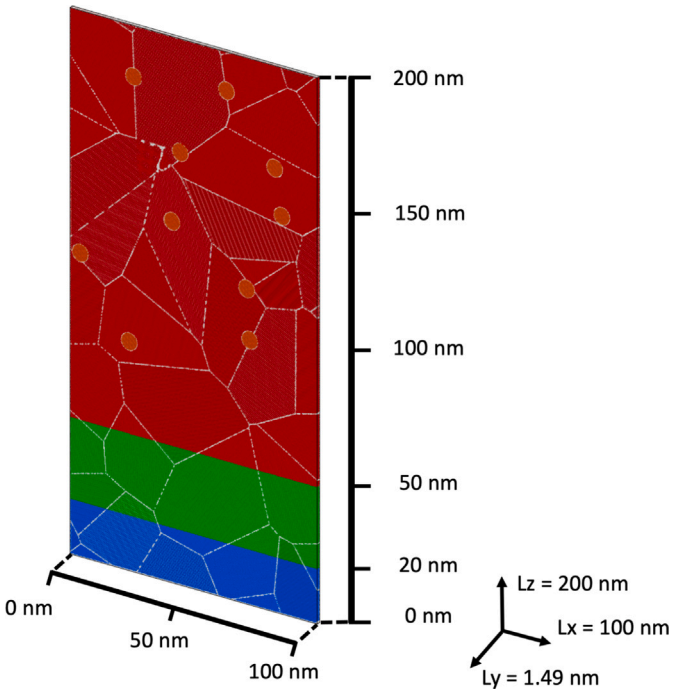

Fig. 1. Schematic of the system in its initial state. The red region, between z = 50 nm and z = 200 nm, represents the laser region. The orange cylinders are the W-NPs. The blue region, between z = 0 nm and z = 20 nm, corresponds to the substrate region. Between the substrate and the laser regions, the region is colored green. The grain boundaries are colored in white. (For interpretation of the references to color in this figure legend, the reader is referred to the web version of this article.)

The thermostat in the substrate region maintains the temperature, allowing solidification to begin via conduction from t = 0 ns. The solidification front progresses gradually, as shown in Fig. 2, by evolving *fcc* fraction profiles and the snapshots taken over time. The *fcc* fraction in the solid region never reaches 1 due to the presence of defects, represented by atoms colored in gray. These defects are more prevalent when located near the solid/liquid interface. The grain boundaries also have a small influence on the *fcc* fraction. Additionally, as indicated in Fig. 2, the rounded hollows precisely pinpoint the locations of W-NPs (*bcc*), which contribute to lowering the *fcc* fraction. However, we estimate the position of the solid/liquid interface using the *fcc* fraction, which equals 0.5. This position also aligns with the curvature observed in the temperature profiles. The corresponding temperature at the interface is estimated at 1160 K, which is very slightly lower than the melting temperature of Cu at 1181 K. Indeed, the temperature gradient in front of the solid/liquid interface is weaker compared to the solid region, but remains positive. The positive temperature gradients in the solid and liquid mean that the heat flux is transferred through the solid, inducing a flat solidification front. The position of the solid/liquid

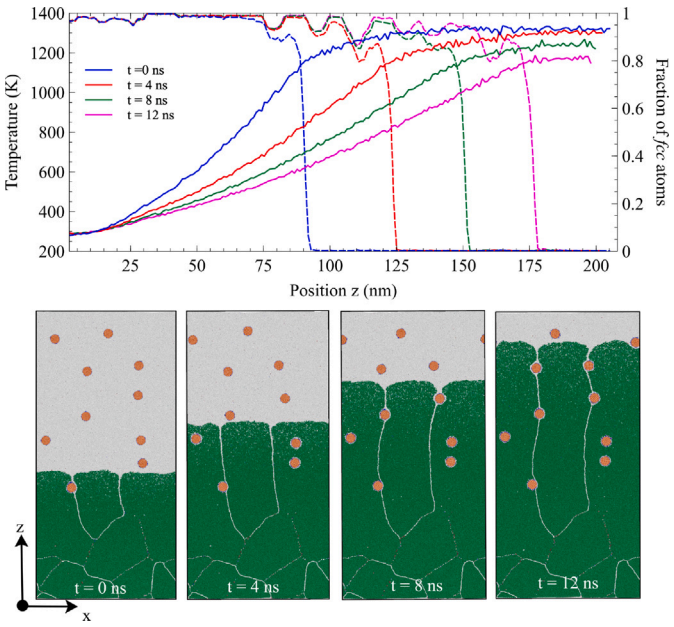

Fig. 2. At top, temperature profiles (solid lines) and the corresponding *fcc* fraction profiles (dashed lines) with respect to the position in the *z*-direction. Snapshots of the system at the times shown at the top (i.e. 0 ns, 4 ns, 8 ns, 12 ns) are presented at the bottom part of the figure. The corresponding color coding: *fcc*-Cu atoms are in green, and *unk*-Cu atoms (unknown or liquid) in light gray. The *bcc*-W and *bcc*-Cu atoms are shown in orange and blue, respectively. (For interpretation of the references to color in this figure legend, the reader is referred to the web version of this article.)

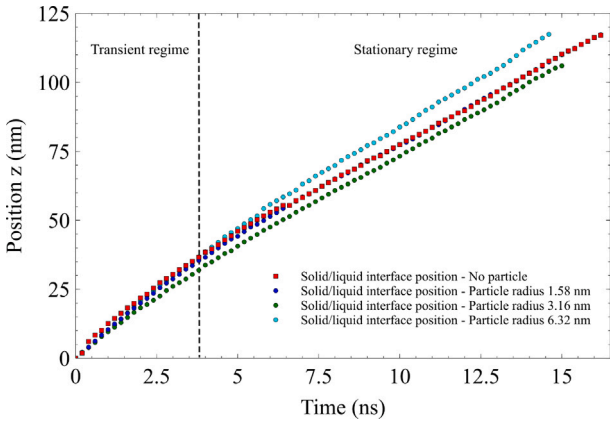

Fig. 3. Solid/liquid interface position in function of the time. In red squares is represented the case without particles (i.e. pure Cu). In blue, green, and cyan circles are represented the cases with particles of size 1.58 nm, 3.16 nm, and 6.32 nm respectively. (For interpretation of the references to color in this figure legend, the reader is referred to the web version of this article.)

interface as a function of time is shown in Fig. 3 for the different simulations with and without particles. Two regimes are observed: transient and stationary state. The transient regime stops at 3.8 ns for simulations with particles, followed by the stationary regime, where the front position evolves linearly. Note that the transient regime for the simulation without particles is slightly longer, up to 6.5 ns. Velocities of the solid/liquid interfaces are extracted in the stationary regime by a linear fit for the different simulations. The simulations without particles and with 1.58 nm particles show a similar velocity equal to 6.40 m/s. The other two simulations with the NP sizes of 3.16 nm and 6.32 nm exhibit a velocity of 6.55 m/s and 7.27 m/s, respectively. As W exhibits an order of magnitude higher thermal diffusivity than copper (see Tables 1 and 2), a higher fraction of W (i.e., bigger W-NPs)

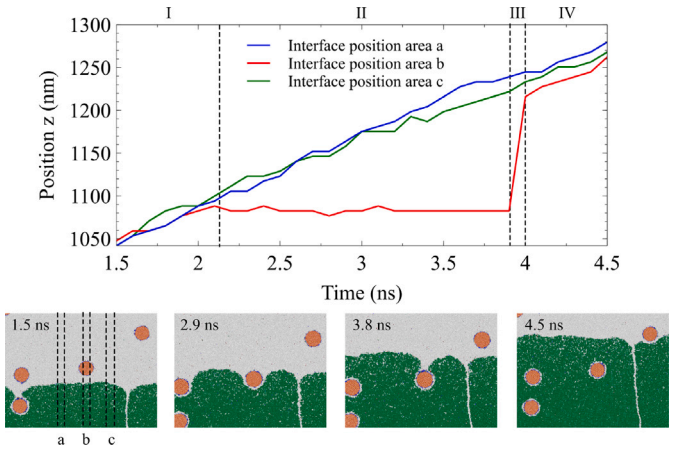

Fig. 4. At top, position of the solid/liquid interface in the *z* direction as a function of time in three different areas around the particle under study. The specific areas (denoted a, b, and c) are shown in the first snapshot at 1.5 ns. Below, snapshots of zoomed-in systems around the particle under study for 4 relevant times (i.e. 1.5 ns, 2.9 ns, 3.8 ns and 4.5 ns) during the engulfment process.

facilitates the heat transfer across the solid/liquid interface, leading to higher solidification front velocities. However, it is important to note that, in reality, Cu and W have a comparable thermal diffusivity near the melting point of copper, minimizing or even reversing such front velocity enhancement effects.

In our simulations, we observed an inflection point in the solidification front as it traverses the nanoparticles (illustrated in Fig. 4). To understand the impact of nanoparticles on the properties of a planar solidification front, we have chosen to focus on a particle located far from grain boundaries. We have isolated a region surrounding this particle, denoted as (b), along with two adjacent zones denoted as (a) and (c), as depicted in the snapshot at 1.5 ns in Fig. 4. The temporal evolution of the positions of the solid/liquid interface within these three zones is depicted in the upper part of Fig. 4. Zones (a) and (c) correspond to regions where the presence of the particle has minimal influence on the solid–liquid interface, whereas zone (b) precisely represents the region where the interface undergoes alteration. By tracking the temporal variation of the *z*-position of the solid–liquid interface, we can delineate four distinct stages:

I. At 1.5 ns, the solid–liquid interface was positioned beneath the particle, as depicted in the 1.5 ns snapshot. The three zones maintained similar positions and velocities, and the interface retained its flatness, seemingly unaffected by the presence of particles. This stage persisted from 1.5 ns to 2.1 ns.
II. By 2.1 ns, the solid–liquid interface in zone (b) had come to a halt, remaining stationary until 3.9 ns. In zones (a) and (c), the front continued to advance with the same velocity observed in Stage I. The snapshot captured at 2.9 ns reveals the concave shape of the interface deformation.
III. Immediately prior to Stage III, the atoms in (b) above the front remain in a liquid or amorphous state, and the trough seems to be narrowing, as illustrated in the 3.8 ns snapshot. Indeed, between 3.9 ns and 4 ns, zone (b) demonstrates a rapid restoration of the solidification front's shape. It reverts from 109 nm to 122 nm in just 0.1 ns. Nevertheless, the position of the front in zone (b), at 4 ns, is located slightly below the front in zones (a) and (c).
IV. In the final Stage IV, the solid–liquid interface in zone (b) gradually aligns itself with the positions observed in zones (a) and (c). However, this adjustment is not fully completed by 4.5 ns and will take place slightly later.

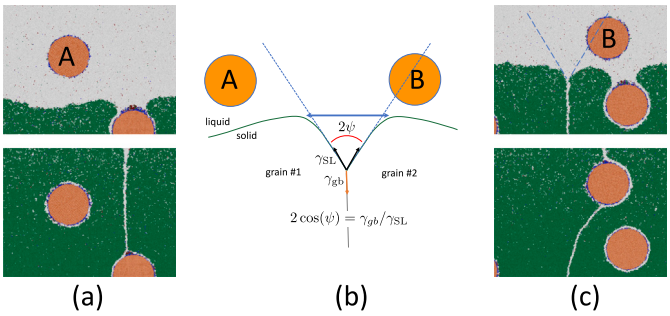

Fig. 5. (a) Engulfment of the NP A by the solidification front. Snapshots at $t = 1.5$ ns (top) and $t = 5.5$ ns (bottom). (b) Schematic representation of the grain boundary grooving at the solid/liquid interface: 2ψ is the grooving angle, γ_{SL} is the solid/liquid interface energy, γ_{gb} is the grain boundary energy. (c) Pinning of the NP by the grain boundary. Snapshots at $t = 2.5$ ns (top) and $t = 5.5$ ns (bottom).

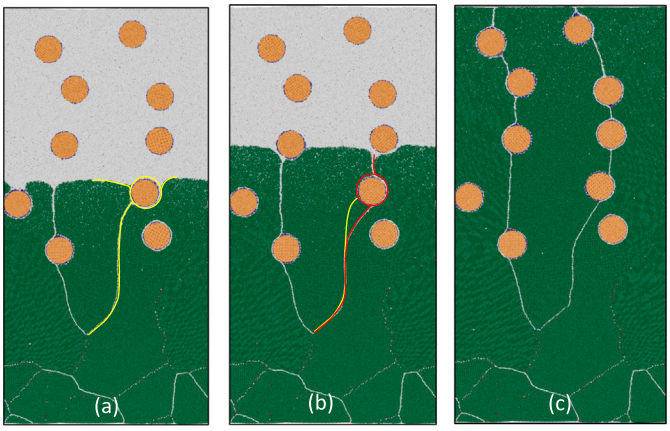

Fig. 6. Snapshots of the system at $t = 4.2$ ns (a) and $t = 6.2$ ns (b) after the entrapment of a NP. The radius of the NP is 6.32 nm. In (a), the grain boundary, the solid/liquid interface, and the ring around the NP are depicted in yellow. In (b), the grain boundary and the ring around the NP are plotted in red. The yellow line indicates the previous position of the grain boundary. (For interpretation of the references to color in this figure legend, the reader is referred to the web version of this article.)

We also observed interesting interactions between W-NPs and Cu grain boundaries. As columnar grains grow in the direction of the imposed temperature gradient, Cu grain boundaries often align themselves accordingly. If W-NPs are sufficiently far away from Cu grain boundaries, the solidification microstructure remains unaffected, as demonstrated in Fig. 5a. However, the planar solid/liquid interface is often disrupted by grain boundary grooves, schematically depicted in Fig. 5b. The grain opening angle, denoted as ψ, reflects the equilibrium between the solid/liquid interfacial energy γ_{SL} and the grain boundary energy γ_{gb}:

$$2\cos(\psi) \times \gamma_{SL} = \gamma_{gb} \tag{1}$$

As demonstrated in Fig. 5c, the W-NP within the grove can attract and pin the corresponding grain boundary, restricting its mobility and subsequent grain growth.

Fig. 6a shows the entire system at the moment when the NP encounters the solid/liquid interface. The grain boundary exhibited a bending behavior to trap the particle. Fig. 6b illustrates the entire system after the passage of the solidification front over the particle. A notable alteration in the grain boundary curvature was observed. Below the NP, the grain boundary endeavored to align tangentially with the particle within the solidified material. On the contrary, above the particle, the grain boundary oriented itself perpendicular to the interface. After complete propagation of the solidification front, most of the W-NPs end up pinning the grain boundaries in this sample due to their proximity to grain boundary grooves at the solidification front; see Fig. 6c.

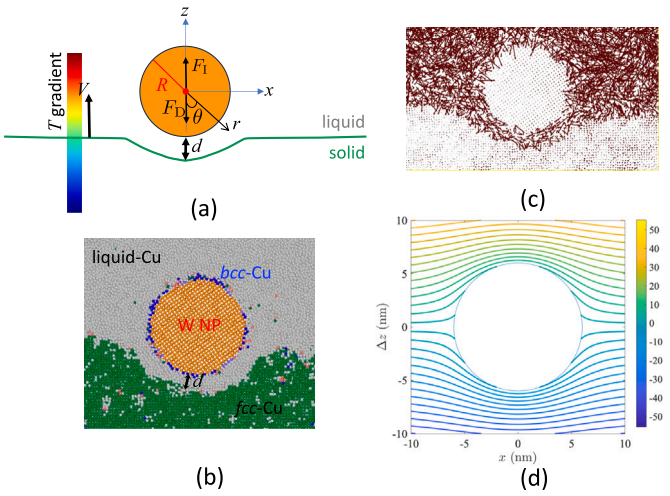

Fig. 7. (a) Schematic representation of a nanoparticle above the solidification front. NP is represented by an orange sphere of radius R. The solid/liquid interface in green moves forward with a velocity V. Distance d measures the separation between the NP and the interface. When gravity is neglected, two forces act on the NP: the drag force F_D and the interfacial force F_I. The system is subjected to a temperature gradient G. The coordinate system used for the calculation of isotherms is (r, θ). (b) Snapshot of a nanoparticle of W above the interface solid/liquid at the beginning of the engulfment process. Color code: *fcc*-Cu atoms are in green, *bcc*-Cu atoms are in blue, *unknown/liquid*-Cu atoms are in light gray, and *bcc*-W atoms are in orange. (c) Displacement vectors (in nanometers) calculated by subtracting the atomic coordinates at $t - 0.1$ ns from those at t ns. (d) Isotherms calculated using Eq. (2). The color bar corresponds to the temperature difference between the temperature field and the reference value at $z = 0$. (For interpretation of the references to color in this figure legend, the reader is referred to the web version of this article.)

To the best of our knowledge, this phenomenon of NP trapping by grain boundary grooves is new and was not previously reported in the literature. However, it is instrumental in the additive manufacturing of metal matrix composites for retaining the fine solidified microstructure during repetitive heating/cooling cycles due to laser printing new layers of material or during the post-process annealing of the 3D printed parts. Thus, further investigation of grain boundary groove interaction with nanoparticles is desired, moving from quasi-2D to real 3D geometry, and isolating the effect of NP size, groove curvature, distance from the groove center to the NP, local temperature distribution, etc. This newly gained knowledge would allow for better control of the solidification microstructure and resulting mechanical performance of nanoparticle-reinforced metal matrix composites.

3.2. Model A — Quantitative assessment

When the solidification front approaches a particle, an interaction occurs between the NP and the advancing front. Fig. 7a schematically illustrates the key characteristics of a NP with a radius of R located above a moving solid–liquid interface. The corresponding snapshot is shown in Fig. 7b. Underneath the particle, the planar front becomes deformed, assuming a concave shape. A narrow gap surrounds the W-NP, filled with a thin layer of liquid copper. The parameter d represents the characteristic length of the liquid layer encircling the NP. Displacement vectors, calculated by subtracting atomic coordinates at $t - 0.1$ ns from those at t ns, are presented in Fig. 7c. This illustrates that atoms located within the layer surrounding the particle can be considered as liquid atoms. Moreover, the system experiences a positive temperature gradient G in the z-direction.

If the heat flow is conductive only, as assumed in [39], the temperature field in the matrix (solid and liquid Cu), T_M, takes the form:

$$T_M - T_0 = -\left[1 + \frac{1-K}{2+K}\left(\frac{R}{r}\right)^3\right] Gr\cos\theta \tag{2}$$

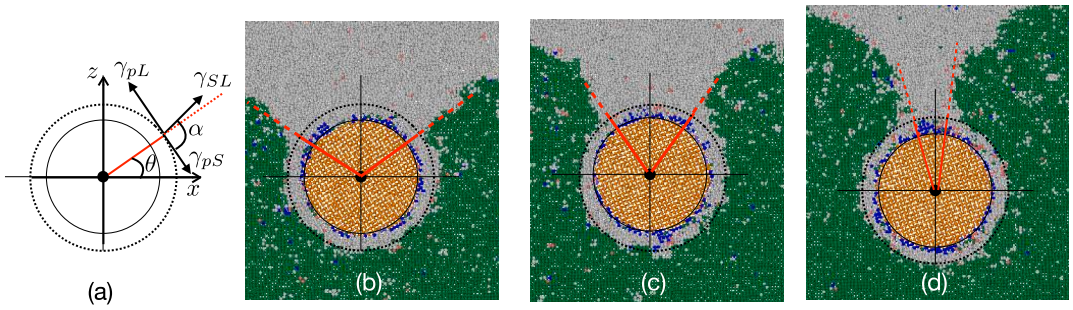

Fig. 8. (a) Schematic representation of a NP during the engulfment process. The solid line corresponds to the NP of radius R; the dashed line delineates the ring of *unk*-Cu around the NP; θ is the polar angle of the contact point between the solid/liquid interface and the NP; γ_{SL} is the solid/liquid interfacial energy, γ_{pL} is the interfacial energy between the particle and the liquid, and γ_{pS} is the interfacial energy between the particle and the solid; α is the angle between γ_{pS} and γ_{SL}. Snapshots of the system during the engulfment process at $t = 1.2$ ns (b), $t = 1.5$ ns (c), and $t = 1.8$ ns (d). The red solid line indicates the direction of the contact point and the dashed line is tangent to the solid/liquid interface. (For interpretation of the references to color in this figure legend, the reader is referred to the web version of this article.)

where (r, θ) is the system coordinates defined in Fig. 7a, $T_0 = (T_M)_{\theta=\pi/2, r\to\infty}$ is the reference temperature and K is the thermal conductivity ratio of the W-NP and Cu-liquid,

$$K = \frac{\kappa_{NP}}{\kappa_M} \equiv \frac{\kappa_{\mathrm{W}}}{\kappa_{\mathrm{Cu}}} \tag{3}$$

In Eq. (3), it is assumed that the thermal conductivities of Cu in the solid and the liquid at a temperature close to the melting point of Cu are equal. The temperature field (2) is illustrated in Fig. 7d with the thermal conductivities of W and Cu as detailed in Tables 1 and 2. The temperature gradient, G, is measured to be 0.4×10^{10} Km^{-1}, while the reference temperature is chosen as $T_0 = 1100$ K, and the NP radius is specified as $R = 6$ nm. The isotherms exhibit a profile similar to that of the solidification front.

The parameter K plays a pivotal role. When K deviates from 1, the isotherms are distorted, indicating the impact of the difference in thermal conductivity between the particle and the matrix. In the scenario where the NP has a lower conductivity than the matrix, represented by $K < 1$, heat flux lines are deflected. Conversely, when $K > 1$, heat flux lines converge toward the NP consistent with the observations made in our simulations.

Different forces act on the NP:

- The dominant force that opposes the particle's displacement by the front is a viscous drag force, denoted as F_{D}. This force is the result of local convective flows around the nanoparticle caused by the approaching solidification front, pushing the nanoparticle toward it. For a spherical particle of radius R close to a planar interface, with $d \ll R$, the drag force reads [40,41]

$$F_{\mathrm{D}} = 6\pi\eta V_{\mathrm{SL}} \frac{R^2}{d} K^2 \tag{4}$$

  where V_{SL} is the solidification front velocity and η is the kinematic viscosity. This form is slightly modified in the case of a non-planar interface [39]. We estimated the drag force acting on a particle of radius $R = 6.32$ nm using the parameters listed in Tables 1 and 2, the measured value of $V_{\mathrm{SL}} = 6.4$ m/s, and a gap thickness between NP and the interface of $d = 0.5$ nm. The resulting attractive drag force is $F_{\mathrm{D}} = 2.5 \times 10^{-6}$ N, which we will compare with another force acting on W-NPs.
- The force often responsible for pushing the NP away from the solidification front is the force coming from the interface free energies [41], F_{I}:

$$F_{\mathrm{I}} = 2\pi R\, \Delta\sigma_0 \left(\frac{d_0}{d_0 + d}\right)^n K \tag{5}$$

  where d_0 is atomic diameter $d_0 = \sqrt[3]{6\Omega/\pi}$, n is an exponent that can have values between 2 and 7, and $\Delta\sigma_0$ is the surface tension difference that can be expressed in terms of interface energy difference:

$$\Delta\sigma_0 = \gamma_{\mathrm{pS}} - \gamma_{\mathrm{pL}} - \gamma_{\mathrm{SL}} \tag{6}$$

  where subscripts p, S, and L denote the nanoparticle, the solid phase, and the liquid phase, respectively. Assuming the local equilibrium at the contact lines between the W-NP and the solid/liquid Cu interface during the engulfment process, Young's equation reads:

$$\gamma_{pS} - \gamma_{pL} = -\gamma_{SL}\cos(\alpha) \tag{7}$$

  where α is the wetting angle of W-NP with solid copper, see Fig. 8a. Figs. 8b–d illustrate the gradual NP engulfment by the solidification front. It is evident that the solid/liquid interface aligns with the direction of the contact point defined by θ and intersects the particle at $\alpha \approx 90°$. This indicates that $\gamma_{pL} \approx \gamma_{pS}$, and only $\Delta\sigma_0 \approx -\gamma_{SL}$ acts on the W-NP. As γ_{SL} is nearly always positive, the negative $\Delta\sigma_0$ means negative interface force i.e., the one that pulls the nanoparticle towards the solidification front, thus promoting the engulfment process. However, compared to the drag force, the interface force is orders of magnitude smaller, with the maximum value of $F_{\mathrm{I}} = -4.7 \times 10^{-9}$ N estimated at $n = 2$ using data from Table 1. Generally speaking, the above analysis shows that any slight wetting of the reinforcement nanoparticles by solid metal would result in a negative interface force that facilitates the engulfment process: $\Delta\sigma_0 = -\gamma_{\mathrm{SL}}(\cos(\alpha) + 1) < 0$ whenever $\cos(\alpha)$ is defined i.e. $\gamma_{pS} < \gamma_{pL} + \gamma_{SL}$. In the other case, the interfacial force will push the NPs in the direction of solidification, away from its front.

Our MD simulations and analysis confirm that W-NPs can be used in the fabrication of copper matrix composites based on interface and drag forces working together towards embedding the nanoparticles into the matrix. In the context of additive manufacturing, the lift force induced by natural convection and coming from the lateral melt flow along the solidification front must also be considered, as it can push NPs away from the solidification front, promoting their aggregation. While such effects are not taken into account in our model system, several atomistic models have been recently proposed to capture melt pool dynamics [35] and microstructure development [42] during laser processing of pure metals, which can be upgraded to study the effect of secondary nanoparticles, being a matter of our future work.

3.3. Model B — Predictions from classical nucleation theory (CNT)

Before we dive into the new simulation set with additional cooling applied to the system, it is important to define our expectations regarding the probability of heterogeneous nucleation in the Cu/W system, which will help us to isolate a specific set of substrate temperatures and cooling rates to reduce computational time while capturing the phenomena of interest. This would also help us isolate areas in which the system's behavior deviates from the CNT predictions.

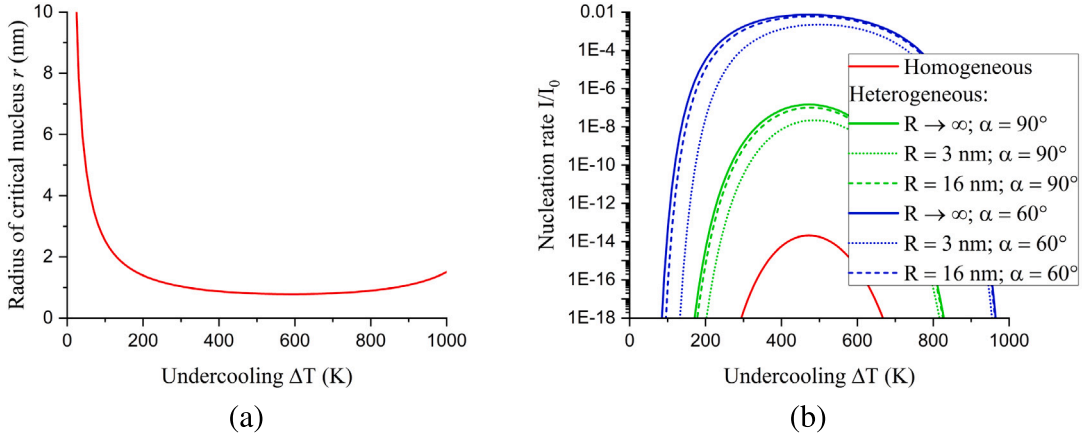

Fig. 9. Critical radius (a) and normalized nucleation rate I/I_0 (Eq. (13)) (b) as a function of the degree of undercooling ΔT.

The first key prediction of CNT is the critical radius of the spherical nuclei overcoming which the nuclei can grow freely. Such a critical radius r is predicted to be the same for both homogeneous and heterogeneous nucleation on flat and curved substrates [43] and depends on the degree of undercooling $\Delta T = T_m - T$ [44]:

$$r = \frac{2\gamma_{SL}}{L_V}\frac{T_m^2}{T\Delta T} \tag{8}$$

Using the data from Table 1, we show in Fig. 9a the dependence of the critical radius on the undercooling degree. We can notice that above just 100 K undercooling, the critical radius drops below a couple of nanometers.

However, the probability of reaching the critical radius is defined by the Gibbs free energy barrier, which can be approximated as [44] :

$$\Delta G_{hom} = \frac{4\pi\gamma_{SL}r^2}{3} = \frac{16\pi\gamma_{SL}^3}{3L_V^2}\frac{T_m^4}{T^2\Delta T^2} \tag{9}$$

The Gibbs free energy barrier for heterogeneous nucleation is often reduced to the fraction of the one corresponding to homogeneous nucleation as only a fraction of critical spherical nuclei is needed on top of the substrate to achieve a free growth stage:

$$\Delta G_{het} = f \cdot \Delta G_{hom} \tag{10}$$

The exact fraction f for the spherical substrate (i.e., nanoparticle) is defined by its radius R (or more precisely the radii ratio $r_r = r/R$ between the critical nuclei and the nanoparticle substrate) as well as the wetting angle of the substrate by the solid phase α [43] :

$$f(r_r,\alpha) = \frac{\left(1+2r_r-\sqrt{1+r_r^2-2r_r\cos\alpha}\right)\cdot\left(-1+r_r+\sqrt{1+r_r^2-2r_r\cos\alpha}\right)^2}{4r_r^3} \tag{11}$$

In the case of $r \ll R$ i.e., $r_r \to 0$, this equation transforms into a well-known expression for heterogeneous nucleation on planar substrate:

$$f(r_r \to 0,\alpha) = \frac{(2+\cos\alpha)\cdot(1-\cos\alpha)^2}{4} \tag{12}$$

According to CNT, after the nucleation barrier ΔG is defined, the nucleation rate I can be expressed as:

$$I = I_0 \exp\left(-\frac{\Delta G}{k_B T}\right) \tag{13}$$

where I_0 is a coefficient that depends on the interface temperature and free energy, and k_B is the Boltzmann constant.

In a previous study, we demonstrated that Classical Nucleation Theory (CNT) was able to predict the main characteristics of homogeneous nucleation in the case of Model B with pure Ni [33] just by looking at the normalized nucleation rate I/I_0. Here, we also look at normalized nucleation rates considering both homogeneous and heterogeneous nucleation on planar and curved substrates. Taking data from Table 1, we plot in Fig. 9b the normalized nucleation rate for homogeneous nucleation and heterogeneous nucleation on the flat substrate and nanoparticles with radii of 3 nm and 16 nm, the range of sizes considered in our MD simulations. Additionally, we consider two wetting angles: $\alpha = 90°$ as determined in the previous subsection for engulfment of nanoparticles, and $\alpha = 60°$ to reflect the fact that heterogeneous nucleation would give preference to the lowest energy interfaces, thus reducing the wetting angle as compared to the interfaces forming during the engulfment process. From Fig. 9b, we first notice how heterogeneous nucleation can drastically reduce the critical undercooling needed to reach some threshold nucleation rate with the wetting angle playing a decisive role in promoting nucleation. At the same time, the reduction in the size of W-NPs would have the opposite effect of increasing the critical undercooling compared to that of the flat substrate. However, because of the relatively small size of critical nuclei, W-NPs with a radius of just 16 nm are sufficient to get close to the flat substrate efficiency. Such observations highlight the importance of selecting nanoparticulate material with low solubility in the matrix to prevent their size reduction at additive manufacturing processing temperatures.

As we formed our expectations regarding this system allowing for the selection of optimal parameters for Model B, one last important remark is about the effect of quasi-2D geometry selected in this work leading to the representation of W-NPs as infinite wires along the y direction due to periodic boundary conditions. The evaluation of heterogeneous nucleation in such a setup was also carried out within CNT leading to quite complex expression for the nucleation barrier, which can be simplified by the following relation: $\Delta G_{plane} < \Delta G_{wire}(R) < \Delta G_{sphere}(R)$ [45]. Due to the inherent stochastic nature of the nucleation process and the relatively low variation in the critical undercooling with R, we can expect no changes in general trends and behavior due to the choice of quasi-2D geometry. Moreover, the threshold nucleation rate is not well defined either and should be calibrated following homogeneous nucleation.

3.4. Model B — Simulation results

In Model B, a systematically implemented global cooling protocol was applied to emulate the thermal dynamics representative of the additive manufacturing of metals. Analogous to its predecessor, Model A, the experimental setup consisted of a substrate maintained at a prescribed temperature denoted T_{sub}, a molten pool, and an intermediary solidified region situated between the substrate and the molten pool, see Fig. 10a. Thermal conditions were characterized by two essential parameters: substrate temperature of 800 K and cooling rate of 215 K/ns. The substrate temperature was chosen to be closer to the

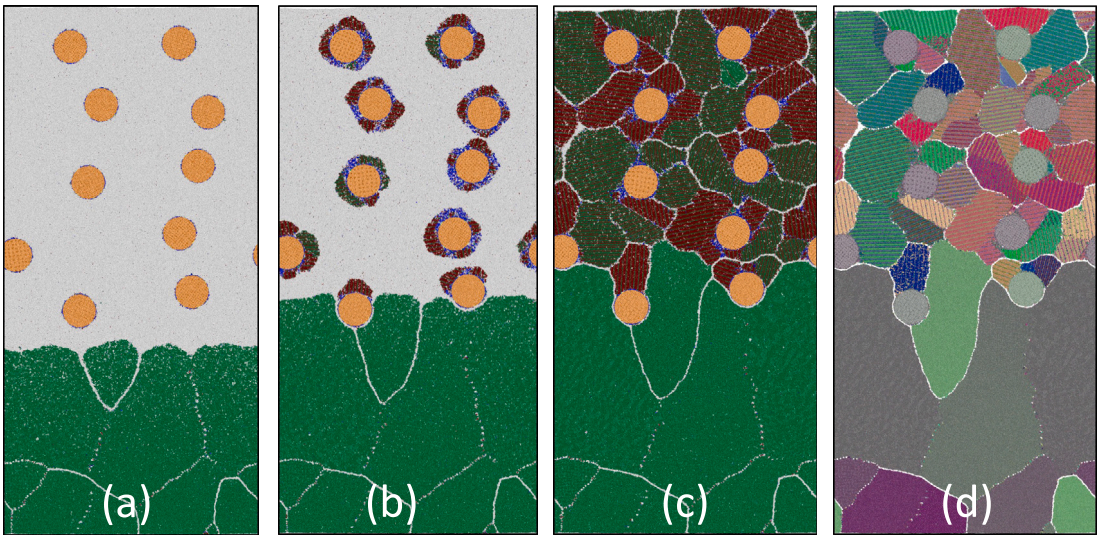

Fig. 10. Snapshots of the system with a NP radius of $R = 20$ lattice units (6.36 nm) submitted to a cooling rate $\alpha = 215$ K/ns with a substrate temperature maintained at $T_{sub} = 800$ K during the solidification process at different times: $t = 0.2$ ns (a), $t = 1$ ns (b), and $t = 1.5$ ns (c,d). (d) The Polyhedral Template Matching (PTM) method [37] enables us not only to identify the atomic structure but also to determine their local lattice orientation (here, an RSMD cutoff of 0.15 was selected). The local orientation is stored as quaternions, which can be translated into RGB color to visualize the lattice orientation through a projection into the Rodrigues space.

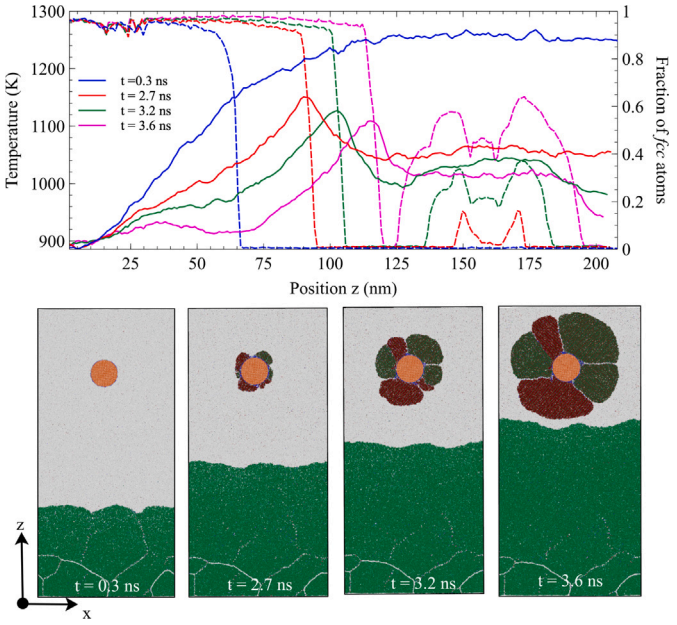

Fig. 11. System (Model B) with a radius of $R = 30$ lattice units (9.54 nm) submitted to a cooling rate $\alpha = 70$ K/ns with a substrate temperature maintained at $T_{sub} = 900$ K. At the top, temperature profiles (solid lines, left axis) and fraction of fcc (dashed lines, right axis) with respect to the position in the z-direction at different times during global cooling. At the bottom, snapshots of the system at 0.3 ns, 2.7 ns, 3.2 ns, and 3.6 ns. Color coding: *fcc*-Cu atoms are in green, *unk*/*liq*-Cu atoms are in light gray, and *bcc*-Cu-atoms are in blue, *bcc*-W atoms are represented in orange. (For interpretation of the references to color in this figure legend, the reader is referred to the web version of this article.)

Cu melting point, essentially slowing the solidification front. Although other sets of parameters were tested, they all led to two outcomes: (1) engulfment of nanoparticles or (2) heterogeneous nucleation before the solidification front reaches the nanoparticles. As the first case was covered in Model A, we focus here on the second case. As shown in Fig. 10b, additional cooling indeed promotes heterogeneous nucleation of Cu grains on the surfaces of tungsten nanoparticles. As expected, such heterogeneous nucleation breaks columnar growth and leads to the formation of fine grains upon complete solidification (see Fig. 10c) with an equiaxed grain structure (see Fig. 10d). As can be seen in Figs. 10b and c, copper grains demonstrate large diversity of crystal structures in the nucleating grains. Although the *bcc* structure (blue) is caused by epitaxial growth on the surface of W, this phase is the most energetically unfavorable and thus limited to a few atomic planes from the interface [16]. At the same time, the most common structure of nucleating grains is composed of nanotwinned *fcc* and *hcp* phases, which is common structure of copper that can be experimentally observed at the nanoscale [46]. Moreover, the difference in cohesive energies between *fcc* and *hcp* phases is quite low (see Table 1), and is even lower between *fcc* and double hexagonal close packed (*dhcp*) phases [16], which is characterized by alternating basal planes with *fcc* and *hcp* structure according to PTM, i.e. the finest nanotwinned structure possible. Because of the extreme variation in local temperature and pressure, as well as the energetics and stress of solid/solid and solid/liquid interfaces at the nanoscale, all such metastable phases are able to form and coexist in solidified material at the early nucleation stages. Retention of such a nanotwinned structure of the copper grains would substantially improve its mechanical performance [11].

Because of the latent heat release during grain nucleation and growth around the nanoparticles, the temperature profiles and grain structure/orientations are challenging to analyze in the sample with multiple nanoparticles. Thus, we move to a more isolated system with a single inoculant particle of different radii introduced into the liquid copper region, as shown in Fig. 11. Furthermore, we also reduce the temperature gradients by increasing the substrate temperature to 900 K, essentially slowing the solidification front to avoid its interactions with a W particle, thus isolating the nucleation process to attribute it to critical undercooling. To measure such undercooling more precisely, we substantially reduce the cooling rate to 70 K/ns, so the trend can be derived with changing nanoparticle size.

The temperature profile and the associated fraction of *fcc* atoms are depicted in Fig. 11 at different moments of time. The W-NP of radius 9.55 nm is located in the liquid region. The time $t = 0$ ns corresponds to the time at which the heat source was released. At time $t = 0.3$ ns, we observed a solidified region ranging from 15 to 65 nm between the thermalized substrate and the solidification front. As in Model A, the position of the solid/liquid interface corresponds to a *fcc*-atom fraction equal to 0.5. The position of the solidification front was thus located at 1175 K, close to the melting point (1181 K).

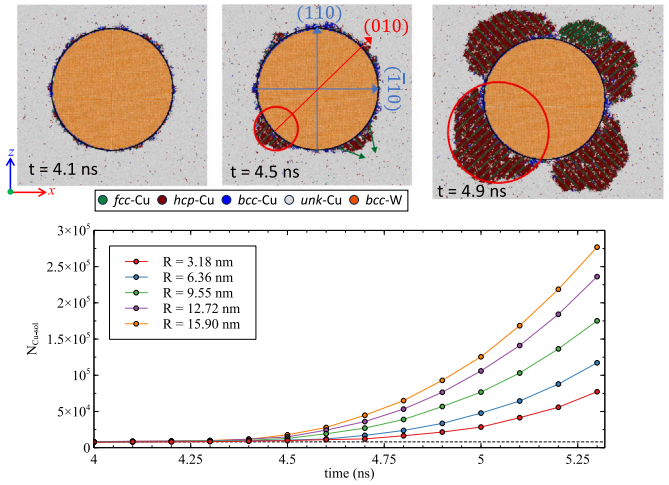

Fig. 12. Top: Snapshots of the system featuring a nanoparticle of tungsten with a radius of $R = 40$ lattice units (12.72 nm), oriented along the (101) direction in the z-axis. Axis in blue indicate the crystallographic orientation of the W-NP. The direction (010) is plotted in red. The green arrows indicate the contact angle of the Cu cap. Bottom: Number of crystallized copper (Cu) atoms, denoted as $N_{\mathrm{Cu-sol}}$, surrounding the NP as a function of time, different NP radii . (For interpretation of the references to color in this figure legend, the reader is referred to the web version of this article.)

The temperature gradient of approximately 5 K/nm established in the solid region, spanning from 15 to 65 nm, was slightly higher than the temperature gradient in the liquid region, ranging from 65 to 100 nm. Because both temperature gradients are positive across the solid/liquid interface, a planar solidification front is expected to propagate through the system without instability. Beyond 100 nm, the temperature is constant.

As soon as cooling became effective (as evidenced by the temperature profile at 2.7 ns), the temperature profile assumed a markedly different shape. The temperature at the solid/liquid interface was approximately 1125 K. The temperature gradient remained positive in the solidified region, while it became negative in the liquid region just above the interface. A temperature hump was observed around the front, associated with the release of latent heat. As depicted in the snapshot at 2.7 ns, we observed nucleation of solid Cu around the W-NP. The temperature of the liquid copper around the NP was 1075 K. At longer times, the Cu solid caps continued to grow, and the solidified copper depicted a flower around the tungsten nanoparticle. This results in a local temperature increase associated with the exothermicity of solidification.

Each cap is made of *fcc* (green) and *hcp* (dark red) atoms. As the difference in cohesive energy per atom for *fcc* and *hcp* is very small (less than 0.011 eV; see Table 1), any thermal fluctuation can cause the formation of *hcp* Cu atoms, resulting in the formation of nanotwinned grains. Moreover, the *hcp* phase could be stabilized by lower-energy interfaces with W-NP compared to the *fcc* phase, and the twin nucleation might be promoted by the disregistry at the incoherent Cu/W interfaces as well as the high surface curvature of the W nanoparticles. The further growth of such nanotwinned *hcp* Cu grains might be further stabilized by periodic boundary conditions and the small size of the system along the y direction, restricting transformation to a more stable *fcc* phase. Nevertheless, we are only interested in the initial nucleation process and do not characterize further growth processes.

The initial stages of heterogeneous nucleation of Cu around W-NP are illustrated in Fig. 12. At 4.1 ns, *bcc*-Cu atoms were identified, forming a thin shell around the nanoparticle. A few moments later (at 4.5 ns), we observed the emergence of two small spherical caps comprising solidified atoms. The centers of these caps are at −45° and −135° relative to the x-direction. In terms of crystallographic directions, these correspond to $(0\bar{1}0)$ and $(\bar{1}00)$. As indicated by the green arrows, the solid caps form a contact angle with the support particle that is less than 90 degrees. The caps continued to expand, maintaining their spherical shape, and two others appeared in the directions (010) and (100). By 4.9 ns, the four caps had completely covered the entire surface of the NP, exhibiting a hemispherical curvature. According to our expectations, the wetting angle between the solid Cu phase and W-NP is well below 90° as indicated by the green arrows in Fig. 12, and is close to 60°. Thus, to interpret the results of our MD simulations in terms of CNT, we should focus on the blue curves in Fig. 9b. The only thing missing for comparison with CNT is the threshold nucleation rate, which can be estimated by comparing CNT predictions for homogeneous nucleation. To do so, we performed Model B simulations without any nanoparticles in the melt and found the first nucleus appearing at the 316 K undercooling, which corresponds to the threshold nucleation rate of the order of 1e−17 in Fig. 9b.

To determine the critical undercooling for the samples with W-NPs, the number of solidified Cu atoms (both in *fcc* and *hcp* structures) around the NPs was monitored over time, as shown in the bottom panel of Fig. 12. It was observed that larger NPs facilitated the nucleation process. Specifically, nucleation occurred at 4.5 ns for NP $R \approx 16$ nm, while a delay in nucleation was noted at 4.75 ns for NP $R \approx 3$ nm. Taking into account the applied cooling rate (70 K/ns after 2 ns in the portion of the system initially at 1250 K), the temperature at which heterogeneous nucleation occurred at the nanoparticle of $R \approx 16$ nm corresponds to the undercooling of 106 K, while for the nanoparticle of $R \approx 3$ nm the undercooling is higher at 120 K, both in line with the CNT predictions (see dashed and dotted blue lines in Fig. 9b).

Fig. 13 shows snapshots of the system at 5.3 ns, for different sizes of the W-NP. We observed 3 caps for R_1 and R_2, 4 caps for R_3 and R_4 and 7 caps for R_5. For R_3 and R_4, some grains consist of contiguous parts of both *fcc* and *hcp* atoms. The size of the inoculants will consequently alter the microstructure of the solidified material. This is illustrated in Fig. 13 (bottom). We observed that the grains on opposite sides exhibit the same lattice orientation. In the case of R_4, we also computed the rotation matrix A for *fcc*-atoms in the different caps. This enables us to calculate the crystal coordinate system $K_{\mathrm{grain}} = \{\vec{e}_1, \vec{e}_1, \vec{e}_1\} = AK_{\mathrm{sample}}$, where $K_{\mathrm{sample}} = \{\vec{1}_x, \vec{1}_y, \vec{1}_z\}$ [47]. We show the vector $\vec{e}_3$ in the snapshots, representing the Miller indices $(hk\ell)$. With the exception of the cap predominantly composed of *fcc*-atoms, variants of the (111) orientation were observed.

An enlarged view of the system with a W-NP of radius 40 l.u. is depicted in Fig. 14, at 4.7 ns, once the heterogeneous nucleation of one spherical cap of Cu became evident. For visualization purposes, a slice of 1.5 Å in the y direction and the upper left quarter of the NP were selected. The external atomic plane #1 of pure W provides a support of 48 Å of length. We observed that *bcc*-Cu atoms align along the planes #1, #2 and #3 of W-NP, allowing for a larger support for the nucleation of Cu. Copper atoms in *bcc* structure have been observed in the first adlayers during the epitaxial growth of Cu on W(110) [48].

Quested and Greer [49] estimated the conditions for the initiation of solid grains in nucleant areas of defined size. Their analysis gives the critical undercooling for the onset of free growth, ΔT_{fg}, as a function of the size r_N of a circular nuclear area:

$$\Delta T_{\mathrm{fg}} = \frac{2\gamma_{\mathrm{sl}}}{L_V}\frac{T_m}{r_N} \tag{14}$$

The critical undercooling for the onset of free growth, ΔT_{fg} corresponding to $r_N = 24$ Å (half the characteristic length of plane #1) is 96 K for the parameters of listed in Table 1. In this estimation, we used the value of γ_{sl} corresponding to *fcc* and liquid copper, which could be different from the interface energy between metastable *hcp* and liquid copper observed in Model B. Heterogeneous nucleation was observed starting from 4.5 ns, corresponding to $\Delta T_{\mathrm{fg}} = 106$ K; therefore, the conditions for free growth of the caps are favorable. After 4.5 ns, we observed an enlargement of the bases of the caps associated with the lateral growth

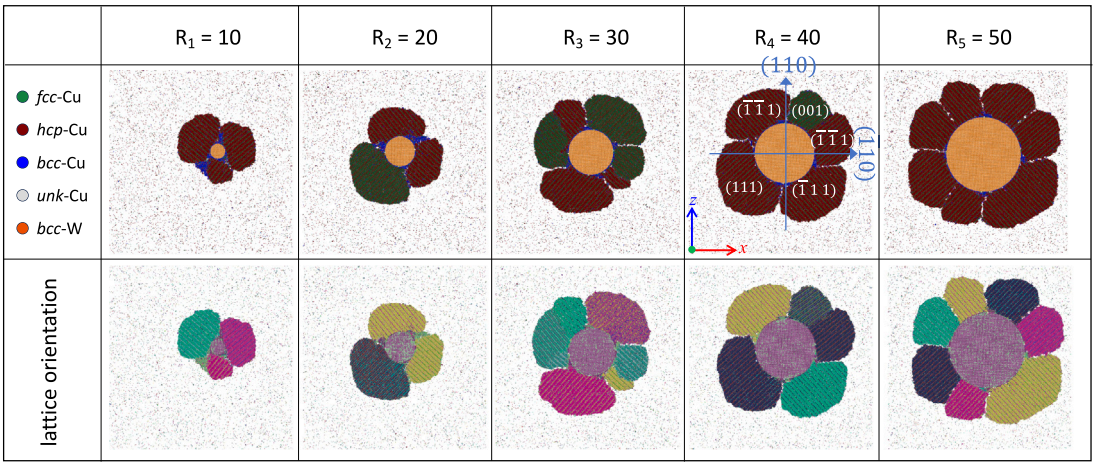

Fig. 13. Snapshots of the system at 5.3 ns for different radii of the W-NP, expressed in lattice units. Atoms are colored according to their structure type or their lattice orientations. The crystallographic orientation of W-NP is (101) along the z direction.

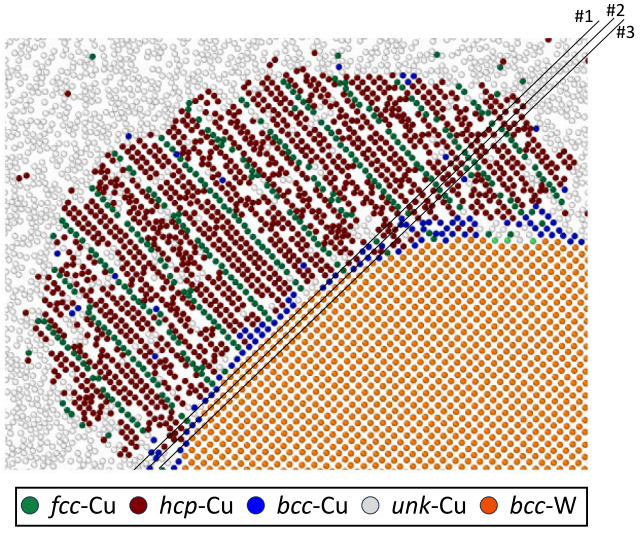

Fig. 14. Snapshot of the system at 4.7 ns with the W-NP having a radius of 40 l.u. with a (101) orientation. Only a slice of 1.5 Å in the y direction, representing one quarter (left, top) of the W-NP, is visualized. Atoms are color-coded based on their structure type. Indexes #1, #2, and #3 correspond to the external planes of the W-NP.

of the grains. This lateral growth may be facilitated by the extent of the nucleant basis. Specifically, *bcc*-Cu atoms aligned along the external planes of W.

In general, we notice substantial interplay between the metastable copper phases and the interface orientation at the initial heterogeneous nucleation stages, the complexity well beyond the original CNT assumptions while considering only the stable *fcc* copper phase (see the green lines in Fig. 9b). At the same time, CNT is capable of not only correctly capturing size dependencies for heterogeneous nucleation but also providing quantitative agreement when metastable phases are taken into consideration. In the latter case, the wetting angle between solid nuclei and the surface of the nanoparticle plays the most important role in predicting the nucleant efficiency in refining the microstructure in additive manufacturing processes. Although state-of-the-art *in situ* experimental techniques are capable of capturing later stages of nucleation and growth [50], atomistic simulations remain the only tool to capture early stages of nucleation at the nanoscale. Recent developments in machine learning methods and tools hold promise to overcome many shortcomings of atomistic simulations associated with limited timescales or low predictive accuracy of the classical interatomic potential [51]. While the former is critical for homogeneous nucleation because of the relatively high nucleation barriers, the latter is the key for heterogeneous nucleation where an accurate description of cross-interface interactions is the biggest challenge. The development of universal machine learning interatomic potentials [52–54] that bring *ab initio* accuracy to the large-scale atomistic simulations while handling the chemical diversity of nucleant/matrix interfaces should enable efficient screening of nucleant materials for any given metal alloy to discover the most promising combinations to be tested experimentally in the future. As we demonstrated here, the simulation of the engulfment process could provide sufficient information to determine the initial wetting angle and to construct the CNT model to predict the range of undercoolings to be tested in various orientations of the substrate. This maximizes the chances of capturing heterogeneous nucleation on MD timescales and refining the CNT model by capturing the most preferable misorientations and phases of the nucleating grains.

4. Conclusions

In continuation of our previous work [33], we employed molecular dynamics simulations to offer *in situ* observations of directional solidification in the context of laser additive manufacturing. These simulations provide a valuable description of processes occurring in a close vicinity of the solidification front. We investigated the solidification of copper with the inclusion of tungsten nanoparticles. Given the minimal solubility between the two metals and the refractory nature of tungsten, W-NPs here play the role of inert inoculants.

We examined the system's behavior following the removal of laser heating. This corresponds to directional solidification in a temperature gradient between the substrate and the liquid region. Because the temperature gradients remain positive in the liquid and solidified regions, the stability of the front was ensured. The presence of W-NPs minimally affected the front velocity compared to that of a system without inoculants. The growth of columnar grains in solidified Cu was observed and the flat solid/liquid interface was slightly deformed by grain boundary grooving. When the flat solid/liquid interface approaches a W-NP, it becomes concave until the solidified copper completely surrounds the NP corresponding to the wetting of the NP by the Cu solid. The evaluation of the magnitude of the forces acting on the NP indicates that the drag force pushing the particle toward the front dominates the interfacial force. Furthermore, since this interfacial force is negative, NP engulfment is facilitated. When the NP is close to the funnel formed by the grain boundary, the particle is trapped by the grain, causing a notable alteration in the curvature of the grain boundary. The final

system corresponds to a particle-reinforced metal matrix composite, with the majority of nanoparticles aligned along grain boundaries.

In the second part of the present work, we investigated the influence of inoculants on the formation of fine equiaxed grains during the solidification process. Classical nucleation theory was used to compare the normalized nucleation rate in the case of homogeneous nucleation with that of heterogeneous nucleation on planar and curved substrates with varying wetting angles. We demonstrated that inoculants facilitate heterogeneous nucleation at moderate melt undercooling as opposed to the one required for homogeneous nucleation. Specifically, the first nucleus appeared at an undercooling of 316 K in the case of homogeneous nucleation. In contrast, copper grains start to form around W-NPs at undercoolings of 120 K for the 3 nm W-NP and 106 K for the 16 nm W-NP. The progress of nucleation in its early stages was also monitored: a thin layer of metastable *bcc*-Cu was formed around the nanoparticle before the appearance of spherical caps whose wetting angle was found to be close to 60°. The quantity of caps increases with the size of the W-NPs.

Our work highlights the importance of wetting of inoculant nanoparticles/strengthening agents by solid metal. Lower wetting angles would lead to increased engulfment by the solidification front, while also increasing nucleation rates and lowering critical undercooling. Because of the microscopic wetting effects and formation of metastable phases on the surface of inoculant nanoparticles, molecular dynamics simulations are essential for the screening and selection of the best inoculant material for each given metal of interest. Our work is setting the basis for such screening, which would become feasible in the near future due to the emergence of universal machine learning force fields bringing *ab initio* accuracy to larger scales.

In the context of the additive manufacturing of W-NP-reinforced copper matrix composites, further research work should focus on the concentration-dependent dispersion of nanoparticles within the melt pool, in particular, at the supercooling zone. The tendency to clustering and agglomeration of W-NPs within molten copper should be carefully evaluated in relation to their size and shape. Although not all of these aspects can be addressed with atomistic simulations, the atomistic details of high-temperature wetting and solidification should be carefully measured to inform microscale and mesoscale multiphysics models of the additive manufacturing process.

CRediT authorship contribution statement

Q. Bizot: Writing – original draft, Investigation, Formal analysis, Data curation. **O. Politano:** Writing – review & editing, Supervision, Software, Resources, Methodology, Funding acquisition. **F. Baras:** Writing – review & editing, Writing – original draft, Visualization, Supervision, Project administration, Funding acquisition. **V. Turlo:** Writing – review & editing, Methodology, Conceptualization.

Declaration of competing interest

The authors declare that they have no known competing financial interests or personal relationships that could have appeared to influence the work reported in this paper.

Acknowledgments

The use of computational facilities at the Computing Center of the University of Bourgogne, DNUM-CCUB, is gratefully acknowledged. V.T. thanks Bern Economic Development Agency for financial support.

References

[1] D. Gu, X. Shi, R. Poprawe, D.L. Bourell, R. Setchi, J. Zhu, Material-structure-performance integrated laser-metal additive manufacturing, Science 372 (2021) eabg1487, http://dx.doi.org/10.1126/science.abg1487.

[2] D. Zhang, D. Qiu, M.A. Gibson, Y. Zheng, H.L. Fraser, D.H. StJohn, M.A. Easton, Additive manufacturing of ultrafine-grained high-strength titanium alloys, Nature 576 (2019) 91–95, http://dx.doi.org/10.1038/s41586-019-1783-1.

[3] J.H. Martin, B.D. Yahata, J.M. Hundley, J.A. Mayer, T.A. Schaedler, T.M. Pollock, 3D printing of high-strength aluminium alloys, Nature 549 (2017) 365–369, http://dx.doi.org/10.1038/nature23894.

[4] A.L. Greer, Overview: Application of heterogeneous nucleation in grain-refining of metals, J. Chem. Phys. 145 (2016) 211704, http://dx.doi.org/10.1063/1.4968846.

[5] B. Lanfant, F. Bär, A. Mohanta, M. Leparoux, Fabrication of metal matrix composite by laser metal deposition - A new process approach by direct dry injection of nanopowders, Materials 12 (2019) 3584, http://dx.doi.org/10.3390/ma12213584.

[6] W.H. Yu, S.L. Sing, C.K. Chua, C.N. Kuo, X.L. Tian, Particle-reinforced metal matrix nanocomposites fabricated by selective laser melting: A state of the art review, Progr. Mater. Sci. 104 (2019) 330–379, http://dx.doi.org/10.1016/j.pmatsci.2019.04.006.

[7] Y.M. Youssef, R.J. Dashwood, P.D. Lee, Effect of clustering on particle pushing and solidification behaviour in TiB_2 reinforced aluminium PMMCs, Composites A 36 (2005) 747–763, http://dx.doi.org/10.1016/j.compositesa.2004.10.027.

[8] M. Roccetti Campagnoli, M. Galati, A. Saboori, On the processability of copper components via powder-based additive manufacturing processes: Potentials, challenges and feasible solutions, J. Manuf. Process. 72 (2021) 320–337, http://dx.doi.org/10.1016/j.jmapro.2021.10.038.

[9] S.T. Auwal, S. Ramesh, F. Yusof, S.M. Manladan, A review on laser beam welding of copper alloys, Int. J. Adv. Manuf. Technol. 96 (2018) 475–490, http://dx.doi.org/10.1007/s00170-017-1566-5.

[10] Y. Liu, J. Zhang, R. Niu, M. Bayat, Y. Zhou, Y. Yin, Q. Tan, S. Liu, J.H. Hattel, M. Li, X. Huang, J. Cairney, Y.-S. Chen, M. Easton, C. Hutchinson, M.-X. Zhang, Manufacturing of high strength and high conductivity copper with laser powder bed fusion, Nature Commun. 15 (2024) 1283, http://dx.doi.org/10.1038/s41467-024-45732-y.

[11] G. Yao, S. Pan, J. Yuan, Z. Guan, X. Li, A novel process for manufacturing copper with size-controlled in-situ tungsten nanoparticles by casting, J. Mater. Process. Technol. 296 (2021) 117187, http://dx.doi.org/10.1016/j.jmatprotec.2021.117187.

[12] T.E.J. Edwards, N. Rohbeck, E. Huszár, K. Thomas, B. Putz, M.N. Polyakov, X. Maeder, L. Pethö, J. Michler, Thermally stable nanotwins: New heights for Cu mechanics, Adv. Sci. 9 (2022) 2203544.

[13] M.N. Polyakov, R.L. Schoeppner, L. Pethö, T.E.J. Edwards, K. Thomas, B. Könnyü, X. Maeder, J. Michler, Direct co-deposition of mono-sized nanoparticles during sputtering, Scr. Mater. 186 (2020) 387–391, http://dx.doi.org/10.1016/j.scriptamat.2020.05.032.

[14] W. Wei, L. Chen, H.R. Gong, J.L. Fan, Strain-stress relationship and dislocation evolution of W-cu bilayers from a constructed n-body W-Cu potential, J. Phys.: Condens. Matter. 31 (2019) 305002, http://dx.doi.org/10.1088/1361-648X/ab1a8a.

[15] J.H. Rose, J.R. Smith, F. Guinea, J. Ferrante, Universal features of the equation of state of metals, Phys. Rev. B 29 (1984) 2963, http://dx.doi.org/10.1103/PhysRevB.29.2963.

[16] N.A. Smirnov, Relative stability of Cu, Ag, and Pt at high pressures and temperatures from ab initio calculations, Phys. Rev. B 103 (2021) 064107, http://dx.doi.org/10.1103/PhysRevB.103.064107.

[17] Z. Jian, K. Kuribayashi, W. Jie, Solid–liquid interface energy of metals at melting point and undercooled state, Mater. Trans. 43 (4) (2002) 721 to 726, http://dx.doi.org/10.2320/MATERTRANS.43.721.

[18] M.J. Assael, A. Chatzimichailidis, K.D. Antoniadis, W.A. Wakeham, M.C. Huber, H. Fukuyamas, Reference correlations for the thermal conductivity of liquid copper, gallium, indium, iron, lead, nickel and tin, High Temp. High Press. 46 (2017) 391–416.

[19] C. Cagran, B. Wilthan, G. Pottlacher, Enthalpy, heat of fusion and specific electrical resistivity of pure silver, pure copper and the binary Ag-28Cu alloy, Thermochim. Acta 445 (2006) 104–110, http://dx.doi.org/10.1016/j.tca.2005.08.014.

[20] E.A. Brandes, G.B. Brook (Eds.), Metal Reference Book, Seventh ed., Butterworth-Heinemann, Oxford, 1992, pp. 14–17.

[21] I.L. Shabalin, Tungsten, in: Ultra-High Temperature Materials I, Springer, Dordrecht, 2014, pp. 237–315, http://dx.doi.org/10.1007/978-94-007-7587-9_3.

[22] Y. Shibuta, S. Sakane, T. Takaki, M. Ohno, Submicrometer-scale molecular dynamics simulation of nucleation and solidification from undercooled melt: Linkage between empirical interpretation and atomistic nature, Acta Mater. 105 (2016) 328–337, http://dx.doi.org/10.1016/j.actamat.2015.12.033.

[23] Y. Shibuta, S. Sakane, E. Miyoshi, S. Okita, T. Takaki, M. Ohno, Heterogeneity in homogeneous nucleation from billion-atom molecular dynamics simulation of solidification of pure metal, Nature Commun. 8 (2017) 10, http://dx.doi.org/10.1038/s41467-017-00017-5.

[24] T. Fujinaga, Y. Shibuta, Molecular dynamics simulation of athermal heterogeneous nucleation of solidification, Comput. Mater. Sci. 164 (2019) 74–81, http://dx.doi.org/10.1016/j.commatsci.2019.03.061.

[25] S. Kavousi, M. Asle Zaeem, Mechanisms of nucleation and defect growth in undercooled melt containing oxide clusters, Acta Mater. 252 (2023) 118942, http://dx.doi.org/10.1016/j.actamat.2023.118942.
[26] T. Yang, X. Han, W. Li, X. Chen, P. Liu, Angular dependent potential for Al-Zr binary system to study the initial heterogeneous nucleation behavior of liquid Al on L12-Al3Zr, Comput. Mater. Sci. 230 (2023) 112480, http://dx.doi.org/10.1016/j.commatsci.2023.112480.
[27] A. Mahata, M. Asle Zaeem, Effects of solidification defects on nanoscale mechanical properties of rapid directionally solidified Al-Cu alloy: A large scale molecular dynamics study, J. Cryst. Growth 527 (2019) 125255, http://dx.doi.org/10.1016/j.jcrysgro.2019.125255.
[28] S. Kumar, S. Nandi, S.K. Pattanayek, M. Madan, B. Kaushik, R. Kumar, K.G. Krishna, Atomistic characterization of multi nano-crystal formation process in Fe-Cr-Ni alloy during directional solidification: Perspective to the additive manufacturing, Mater. Chem. Phys. 308 (2023) 128242, http://dx.doi.org/10.1016/j.matchemphys.2023.128242.
[29] Y. Shibuta, M. Ohno, T. Takaki, Advent of cross-scale modeling: High-performance computing of solidification and grain growth, Adv. Theory Simul. 1 (2018) 1800065, http://dx.doi.org/10.1002/adts.201800065.
[30] S. Kavousi, B.R. Novak, D. Moldovan, M. Asle Zaeem, Quantitative prediction of rapid solidification by integrated atomistic and phase-field modeling, Acta Mater. 211 (2021) 116885, http://dx.doi.org/10.1016/j.actamat.2021.116885.
[31] S. Kavousi, A. Gates, L. Jin, M. Asle Zaeem, A temperature-dependent atomistic-informed phase-field model to study dendritic growth, J. Cryst. Growth 579 (2022) 126461, http://dx.doi.org/10.1016/j.jcrysgro.2021.126461.
[32] S. Kavousi, V. Ankudinov, P.K. Galenko, M. Asle Zaeem, Atomistic-informed kinetic phase-field modeling of non-equilibrium crystal growth during rapid solidification, Acta Mater. 253 (2023) 118960, http://dx.doi.org/10.1016/j.actamat.2023.118960.
[33] Q. Bizot, O. Politano, V. Turlo, F. Baras, Molecular dynamics simulations of nanoscale solidification in the context of Ni additive manufacturing, Materialia 27 (2023) 101639, http://dx.doi.org/10.1016/j.mtla.2022.101639.
[34] see http://lammps.sandia.gov/, S. Plimpton, Fast parallel algorithms for short-range molecular dynamics, J. Comput. Phys. 117 (1995) 1, http://dx.doi.org/10.1006/jcph.1995.1039.
[35] O. Politano, F. Baras, Thermocapillary convection in a laser-heated Ni melt pool: A molecular dynamics study, J. Appl. Phys. 134 (2023) 095301, http://dx.doi.org/10.1063/5.0167061.
[36] A. Stukowski, Visualization and analysis of atomistic simulation data with OVITO-the open visualization tool, Modelling Simul. Mater. Sci. Eng. 18 (2010) 015012, http://dx.doi.org/10.1088/0965-0393/18/1/015012.
[37] P.M. Larsen, S. Schmidt, J. Schiøtz, Robust structural identification via polyhedral template matching, Modelling Simul. Mater. Sci. Eng. 24 (2016) 055007, http://dx.doi.org/10.1088/0965-0393/24/5/055007.
[38] P. Hirel, Atomsk: A tool for manipulating and converting atomic data files, Comput. Phys. Comm. 197 (2015) 212–219, http://dx.doi.org/10.1016/j.cpc.2015.07.012.
[39] D. Shangguan, S. Ahuja, D.M. Stefanescu, An analytical model for the interaction between an insoluble particle and an advancing solid/liquid interface, Metall. Mater. Trans. A 23A (1992) 669–680, http://dx.doi.org/10.1007/BF02801184.
[40] D.R. Uhlmann, B. Chalmers, K.A. Jackson, Interaction between particles and a solid–liquid interface, J. Appl. Phys. 35 (1964) 2986–2993, http://dx.doi.org/10.1063/1.1713142.
[41] D.M. Stefanescu, F.R. Juretzko, D.K. Dhindaw, A. Catalina, A. Sen, P.A. Curreri, Particle engulfment and pushing by solidifying interfaces: Part II. Microgravity experiments and theretical analysis, Metall. Trans. 29A (1998) 1697–1706, http://dx.doi.org/10.1007/s11661-998-0092-3.
[42] S. Kurian, R. Mirzaeifar, Selective laser melting of aluminum nano-powder particles, a molecular dynamics study, Addit. Manuf. 35 (2020) 101272, http://dx.doi.org/10.1016/j.addma.2020.101272.
[43] M. Iwamatsu, Line-tension effects on heterogeneous nucleation on a spherical substrate and in a spherical cavity, Langmuir 31 (2015) 3861–3868, http://dx.doi.org/10.1021/la504926s.
[44] K.F. Kelton, Crystal nucleation in liquids and glasses, in: Solid State Physics, Elsevier, 1991, pp. 75–177, http://dx.doi.org/10.1016/S0081-1947(08)60144-7.
[45] L. Hu, H. Lu, X. Ma, X. Chen, Heterogeneous nucleation on surfaces of the three-dimensional cylindrical substrate, J. Cryst. Growth 575 (2021) 126340, http://dx.doi.org/10.1016/j.jcrysgro.2021.126340.
[46] L. Sun, X. He, J. Lu, Nanotwinned and hierarchical nanotwinned metals: a review of experimental, computational and theoretical efforts, Npj Comput. Mater. 4 (2018) 6, http://dx.doi.org/10.1038/s41524-018-0062-2.
[47] V. Turlo, O. Politano, F. Baras, Alloying propagation in nanometric Ni/Al multilayers: A molecular dynamics, J. Appl. Phys. 121 (2017) 055304, http://dx.doi.org/10.1063/1.4975474.
[48] K. Reshöft, C. Jensen, U. Köhler, Atomistics of the epitaxial growth of cu on w(110), Surf. Sci. 421 (1999) 320–336, http://dx.doi.org/10.1016/S0039-6028(98)00859-0.
[49] T.E. Quested, A.L. Greer, Athermal heterogeneous nucleation of solidification, Acta Mater. 53 (2005) 2683–2692, http://dx.doi.org/10.1016/j.actamat.2005.02.028.
[50] E. Liotti, C. Arteta, A. Zisserman, A. Lui, V. Lempitsky, P.S. Grant, Crystal nucleation in metallic alloys using x-ray radiography and machine learning, Sci. Adv. 4 (2018) eaar4004, http://dx.doi.org/10.1126/sciadv.aar4004.
[51] E.R. Beyerle, Z. Zou, P. Tiwary, Recent advances in describing and driving crystal nucleation using machine learning and artificial intelligence, Curr. Opin. Solid State Mater. Sci. 27 (2023) 101093, http://dx.doi.org/10.1016/j.cossms.2023.101093.
[52] C. Chen, S.P. Ong, A universal graph deep learning interatomic potential for the periodic table, Nat. Comput. Sci. 2 (2022) 718–728, http://dx.doi.org/10.1038/s43588-022-00349-3.
[53] S. Takamoto, C. Shinagawa, D. Motoki, K. Nakago, W. Li, I. Kurata, T. Watanabe, Y. Yayama, H. Iriguchi, Y. Asano, T. Onodera, T. Ishii, T. Kudo, H. Ono, R. Sawada, R. Ishitani, M. Ong, T. Yamaguchi, T. Kataoka, A. Hayashi, N. Charoenphakdee, T. Ibuka, Towards universal neural network potential for material discovery applicable to arbitrary combination of 45 elements, Nature Commun. 13 (2022) 2991, http://dx.doi.org/10.1038/s41467-022-30687-9.
[54] D.P. Kovács, I. Batatia, E.S. Arany, G. Csányi, Evaluation of the MACE force field architecture: From medicinal chemistry to materials science, J. Chem. Phys. 159 (2023) 044118, http://dx.doi.org/10.1063/5.0155322.